Weyl semimetal phases and implementation in degenerate optical cavities

Bo Ye Sun, Xi Wang Luo, Ming Gong,* Guang Can Guo, and Zheng Wei Zhou†
Key Laboratory of Quantum Information, University of Science and Technology of China, CAS, Hefei, Anhui 230026, People's Republic of China
and Synergetic Innovation Center of Quantum Information and Quantum Physics, University of Science and Technology of China, Hefei, Anhui 230026, People's Republic of China
(Received 24 March 2017; published 31 July 2017)

We propose a scheme for simulating the behaviors of Weyl semimetals by using a two-dimensional array of degenerate optical cavities. To simplify such a three-dimensional system to a two-dimension system, the orbital angular momentum of the light is used to support an extra synthetic dimension. We find that this system is quite suitable for the purpose of investigating the features of the Weyl point by taking advantage of the input-output relation of the optical cavity system. We show that the transport properties of our system are determined by the number of sites along the constrained direction and the spin texture of the system makes the transport momentum dependent and spin dependent.

DOI: 10.1103/PhysRevA.96.013857

I. INTRODUCTION

The Weyl semimetal phase has attracted much attention in recent years for its novel gapless band structure in the bulk and exotic Fermi arcs on the surface. Historically, this phase can be traced back to Hermann Weyl in 1929 as a special solution to the Dirac equation, which plays a fundamental role in quantum field theory and particle physics. Recently great interest in the Weyl semimetal phase has arisen from the possibility of realization of this phase using quasiparticles in certain condensed matter systems or, much more broadly in the context of quantum simulation, from the realization of synthetic models supporting Weyl semimetal phases using other systems. Theoretically, this phase has been predicted in various solid materials since 2011 [1–5], and the first experimental verification of this phase was reported in TaAs material in 2015 [6,7]. First-principle calculation has played an important role in unveiling a number of solid materials as potential Weyl semimetal candidates [8–10]. Nevertheless, in these materials, the related energy spectrum is generally very complicated and their unique topological boundary states, i.e., the Fermi arc, may be fully embedded in the bulk spectrum. The concept of an ideal Weyl semimetal recently proposed in Ref. [8] is rare in nature, and it makes the analysis of the properties of the Weyl semimetals, including the spin texture of the boundary states, the flat bands, and the transport properties, quite difficult [11,12].

To investigate the features of the Weyl point, some artificial simulators are proposed in photonics [13–17], plasmonics [18,19], acoustics [20,21], and circuit-QED lattice systems [22]. Recently, to overcome the difficulty of exploring Weyl point physics, several groups have proposed some theoretical schemes to simulate Weyl-type topological matter in a planar two-dimensional (2D) geometry [23,24] by virtue of a synthetic dimension in the form where internal degrees of freedom of the system mimic the third spatial dimension [25–28]. Here, the approach of a synthetic dimension refers to mapping discrete internal degrees of freedom of matters, such as atomic gases [25,26,28–35] and photonics [27,36–41], to labeling lattice sites along an additional synthetic dimension. By adjusting the effective tunneling between the virtual sites one can simulate the particles' move along this extra dimension.

In this work, we provide a bottom-up construction of 3D Weyl-type matter using a 2D array of degenerate optical cavities [42–44], in which one of the extra dimensions is simulated using the orbital angular momentum (OAM) of light [27]. The OAM-carrying beams have an azimuthal phase dependence with an integer OAM number, which can be manipulated and measured with high precision [45–47] and can be even taken advantage of generating high-dimensional entangled states [48,49]. Here, the degree of freedom of the OAM can serve as a synthetic dimension and a d-spatial dimensional cavity crystal can be used to simulate $(d+1)$-dimensional physics. Besides immensely reducing the design complexity, here we specify that the particular probing method in the degenerated cavities array will contribute to unveiling the properties of the Weyl point such as transmission properties and spin textures. Furthermore, we also investigate the effect of finite sizes in the constrained direction, which implies that the Fermi arc can be observed by using only a few degenerated cavities.

II. MODEL AND PHASE DIAGRAM

The model considered here can be written as

$$H = \sum_{l} [\phi_l^\dagger i t_{xy} \sigma^x \phi_{(l_x+1,l_y-1,l_z)} + \phi_l^\dagger i t_y \sigma^y \phi_{(l_x,l_y+1,l_z)} - t_z \phi_l^\dagger \sigma^z \phi_{lx,ly,lz+1} + t_z' \phi_l^\dagger \sigma^z \phi_l] + \text{H.c.}, \quad (1)$$

where $l = (l_x, l_y, l_z)$ stands for the site index (l_x, l_y) and the OAM index l_z; t_{xy} and t_y are the hopping energy along the xy ([110]) and y ([010]) directions, respectively; t_z is the hopping along the synthetic dimension z; t_z' is the on-site spin-splitting energy; $\sigma^{x,y,z}$ are the Pauli matrices; and $\phi_l = (\phi_{l\uparrow}, \phi_{l\downarrow})^T$ is the wave function with spin $\uparrow$ and $\downarrow$, encoded by the horizontal and vertical polarization of light.

*gongm@ustc.edu.cn
†zwzhou@ustc.edu.cn

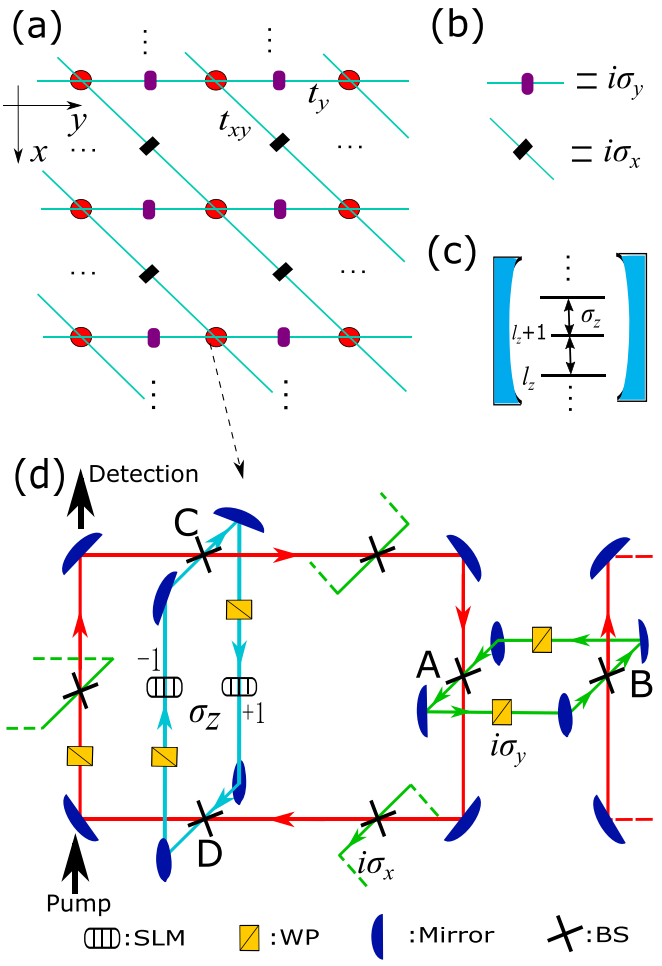

FIG. 1. Schematics on simulating the Weyl semimetal phase based on degenerate optical cavities. (a) Realization of the Weyl semimetal phase using two-dimensional degenerate cavities. Red circles refers to degenerated optical cavities. (b) The hopping between the neighboring sites and their corresponding spin-dependent hopping term. (c) The spin-dependent hopping term along the z direction emulated using the OAM of light. (d) The physical implementation of the degenerate cavity. SLM, WP, and BS represent spatial light modulator, wave plate, and beam splitter, respectively. The black arrows stand for the pump and detection processes.

This model bears resemblance to the three-dimensional tight-binding model for Weyl semimetals in solid materials. Nevertheless, in this work, this three-dimensional structure can be realized by using an array of two-dimensional degenerate cavities, as schematically shown in Fig. 1(a). We first focus on the first two terms in Eq. (1), which are rather similar to the spin-orbit coupling and are essential for the realization of topological phases in insulators and superconductors. These two terms require the spin flipping during the hopping between the neighboring sites. In particular, along the y direction, the transition between spin up (down) and spin down (up) should differ by a relative π phase for the realization of $i\sigma_y$ coupling. This can be realized by using the experimental scheme shown as the green circuit (which connects A and B) in Fig. 1(d). The two beam splitters (shown as BS in the figure) located at A and B in the two main cavities are connected by a small loop, in which the photon from A $\rightarrow$ B and B $\rightarrow$ A can travel in two different paths, and thus can feel totally different relative phases. Moreover, in each path, a wave plate (WP) is added. This WP is a birefringent material, which rotates the horizontal and vertical polarization (i.e., "spin" in our model) of the light as $e^{i\alpha\cdot\sigma}$. Here, $\alpha = (\alpha_x,\alpha_y,\alpha_z)$ is determined by the Jones matrices [27,50] of the corresponding wave plates. Thus, by choosing $\alpha = (0, \pm\pi/2, 0)$ in each path, one can realize the simplest spin-orbit coupling in solid materials. The hopping along the xy direction can also be realized in a similar way except that now $\alpha = (\pm\pi/2, 0, 0)$; thus we have the $\pm i\sigma_x$ coupling. It should be noted that the lengths of the auxiliary cavities are chosen for destructive interference and that the lengths of the main cavities are constructive; thus most of the light still remains in the main cavities in our model [27].

To simulate Weyl semimetal phases, in addition to these two spin-flipped in-plane hopping terms, we need a σ_z-type hopping term along the third dimension, which will be simulated by the synthetic dimension constructed by the clock-circulating OAM. If the cavity is well designed, these photons with different angular momenta will essentially have the same energy. Thus each cavity in Fig. 1(a) is dubbed a degenerate cavity [42–44]. This represents an essential difference between the OAM and the angular momentum in atoms. As a consequence, the t_z and t_z' terms in Eq. (1) are independent of the angular momentum index l_z. To simulate the σ_z hopping between the OAM states, a new auxiliary cavity (light blue circuit) connecting the two points C and D in Fig. 1(d) is required. Similar to the loop between A and B, we require that the left-half cavity and right-half cavity can travel along different paths in the auxiliary cavity, in which these two paths are controlled by two different spatial light modulators (SLM) to increase or decrease the OAM by one unit. The SLMs are simple spiral phase plates, which change the OAM of photons by ± 1 and hence simulate the hopping in the z direction. The corresponding experimental implementation can be found in Refs. [51,52]. Along these two beams, two additional WPs are required to introduce a relative π phase for the spin-up and spin-down light, for the purpose of realizing the $t_z\sigma_z$ term. It is also feasible to introduce an effective Zeeman field term denoted by t_z' in our model, which can be realized by adding a WP in the main photon path (the red circuit in Fig. 1(d)) in the main cavity. By using such kind of construction, the parameters t_{xy}, t_y, t_z, and t_z' can all be tuned by the optical elements. More detailed discussions can be found Appendix A.

This scheme fulfills the construction of the Weyl semimetal phase from the bottom-up design. To understand the property of the Weyl points in the model, we transform the Hamiltonian to the momentum space in an idealized infinite optical cavity array,

$$\mathcal{H}(\mathbf{k}) = \sum_{\mathbf{k}} \phi_{\mathbf{k}}^{\dagger}[\epsilon_{\mathbf{k}} + d_{\alpha}(\mathbf{k})\sigma^{\alpha}]\phi_{\mathbf{k}}, \tag{2}$$

where $d_x = 2t_{xy}\sin(k_x - k_y)$, $d_y = 2t_y \sin k_y$, $d_z = 2t_z \cos k_z - 2t_z'$, and $\epsilon_{\mathbf{k}} = 0$, with $-\pi \leqslant k_i \leqslant \pi$ for $i = x$, y, and z. The energy gap between the upper band and the lower band can be written as

$$E_{\mathbf{k}} = 2\sqrt{d_x^2 + d_y^2 + d_z^2},$$

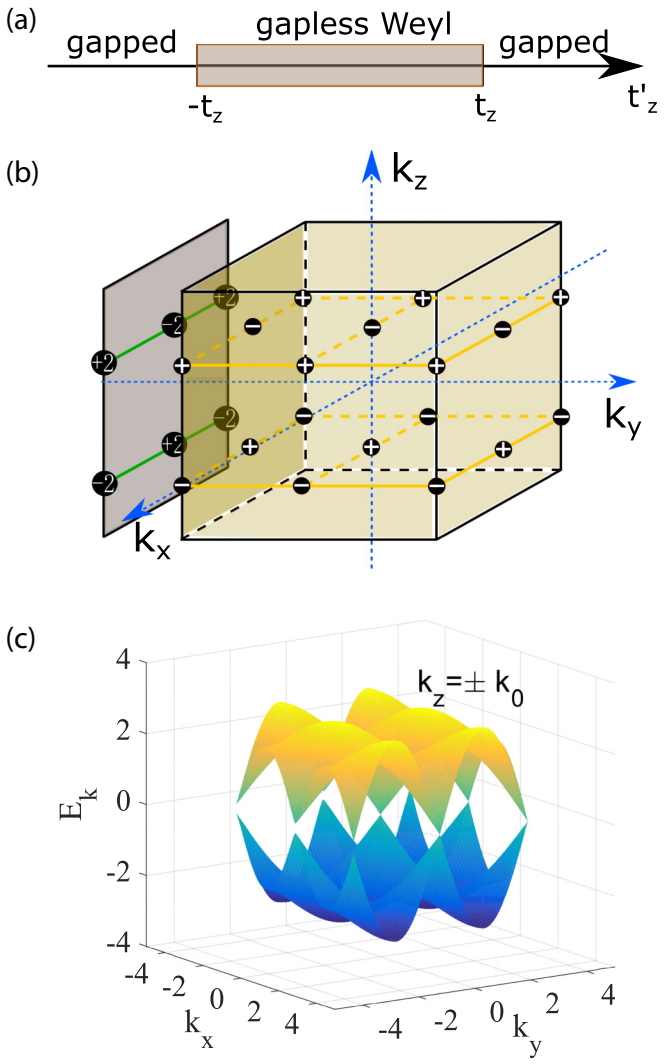

FIG. 2. Distribution of the Weyl point and the band structure. (a) The phase where the Weyl point exits with the varying of t_z'. (b) The distribution of the Weyl point in the momentum space. The topological charges of each Weyl point are shown in the figure. The dots with $+2$ or -2 are the projection of Weyl points in the k_x-k_z plane. The green lines are the theoretically obtained Fermi arcs. (c) The band structure when the Weyl point exits with $k_z = \pm k_0$.

which is always fully gapped when $|t_z'| > |t_z|$. For the sake of simplicity, hereafter let us assume $t_z > 0$. The phase diagram for this model is presented in Fig. 2(a). In between the two gapped phases, $|t_z'| < t_z$ (i.e., the shadow area in the figure), let us assume $t_z' = t_z \cos(k_0)$; thus all the gapless Weyl points can be found in $k_z^w = \pm k_0$, $k_y^w = 0, \pm\pi$ and $k_x^w = k_y^w, k_y^w \pm \pi$. This model has an inversion symmetry defined as $\mathcal{I} = \sigma_z$, through which we find $\sigma_z \mathcal{H}(\mathbf{k})\sigma_z = \mathcal{H}(-\mathbf{k})$. If we expand the Hamiltonian around one of the gapless Weyl points, we obtain $\mathcal{H}_{k^w}(\mathbf{k}) = v_{ij}(\mathbf{k^w})(k_i - k_i^w)\sigma_j$, where

$$v(\mathbf{k^w}) = \begin{pmatrix} 2s_1 t_{xy} & 0 & 0 \\ -2s_1 t_{xy} & 2s_2 t_y & 0 \\ 0 & 0 & -2s_3 t_z \end{pmatrix}. \tag{3}$$

Here, $s_1 = \cos(k_x^w - k_y^w)$, $s_2 = \cos(k_y^w)$, and $s_3 = \sin(k_z^w)$ are determined by the location of the Weyl points k_i^w. Then $\sigma_z \mathcal{H}_{k^w}(\mathbf{k})\sigma_z = v_{ij}(-\mathbf{k^w})(-k_i + k_i^w)\sigma_j = \mathcal{H}_{-k^w}(-\mathbf{k})$. The chirality, or topological charge, of the Weyl point is defined as $\nu(\mathbf{k^w}) = \text{sign}\{\det[v(\mathbf{k^w})]\}$, then we find

$$\nu(\mathbf{k^w}) = \text{sign}[-s_1 s_2 s_3 t_{xy} t_y t_z]. \tag{4}$$

This result demonstrates the possibility of changing the chirality of the Weyl points by controlling s_i, i.e., the location of the Weyl points. Moreover, we find

$$\nu(-\mathbf{k^w}) = -\nu(\mathbf{k^w}). \tag{5}$$

This symmetry ensures that the two Weyl points with opposite momenta should have opposite chirality. Notice that the Weyl points in this model are rather robust due to the involvement of all Pauli matrices in the effective Hamiltonian. In fact, introducing other types of couplings in Fig. 1(a) will not immediately destroy these phases, provided the Weyl points with opposite chiralities are not confused. The introduction of these extra terms can only slightly shift the position of the Weyl points.

III. OPTICAL TRANSMISSION SPECTRA

Our system has the advantage of exciting the bulk states (Dirac cones) or edge states (Fermi arcs) individually due to the simple band structure presented in Fig. 2(c). In the following we demonstrate the measurement of these states using the optical transmission spectra by tuning the energy of the input light. This is essentially analogous to initiating quantum transport formulism in solid materials by tuning the chemical potential of electrons.

The transmission can be obtained from the output field amplitude of the detection process D_l^{DO} and the input field amplitude of the pump process D_l^{PI} of the light at site l (see Fig. 1), which are calculated from the Langevin equations of the system [27,53]:

$$\dot{\phi}_l = -i[\phi_l, H] - \sqrt{\gamma_l^{\text{D}}} D_l^{\text{DO}} - \sqrt{\gamma_l^{\text{P}}} D_l^{\text{PO}} - \sqrt{\gamma_l^{\text{dis}}} D_l^{\text{dis}} + (\gamma_l^{\text{P}} + \gamma_l^{\text{D}} + \gamma_l^{\text{dis}})\phi_l/2, \tag{6}$$

$$\dot{\phi}_l = -i[\phi_l, H] - \sqrt{\gamma_l^{\text{P}}} D_l^{\text{PO}} - \sqrt{\gamma_l^{\text{dis}}} D_l^{\text{dis}} + (\gamma_l^{\text{P}} - \gamma_l^{\text{D}} + \gamma_l^{\text{dis}})\phi_l/2, \tag{7}$$

$$\dot{\phi}_l = -i[\phi_l, H] - \sqrt{\gamma_l^{\text{P}}} D_l^{\text{PI}} - (\gamma_l^{\text{P}} + \gamma_l^{\text{D}} + \gamma_l^{\text{dis}})\phi_l/2. \tag{8}$$

Here, the dissipation of the light due to the reflection of the mirrors is represented by D_l^{dis}, and the reflection of the pump process is represented by D_l^{PO}. The parameters $\gamma_l^{\text{P/D/dis}}$ are the loss rates due to the pump, detection processes, and dissipation, respectively. Then by a Fourier transformation of the above equations we find

$$\sqrt{\gamma_l^{D}} D_l^{\text{DO}}(\omega) = \gamma_l^{\text{D}} \phi_l(\omega), \tag{9}$$

$$\sqrt{\gamma_l^{P}} D_l^{\text{PI}}(\omega) = (i\omega - \gamma_l/2)\phi_l(\omega) - i \sum_{l'} H_{l,l'} \phi_{l'}(\omega), \tag{10}$$

Here $\gamma_l = \gamma_l^{\mathrm{D}} + \gamma_l^{\mathrm{P}} + \gamma_l^{\mathrm{dis}}$ and $H = \sum_{l,l'} \phi_l^\dagger H_{l,l'} \phi_{l'}$. Thus, the transmission coefficient is obtained as

$$t_{l_1,l_2}(\omega) = \frac{D_{l_1}^{\mathrm{DO}}(\omega)}{D_{l_2}^{\mathrm{PI}}(\omega)} = \langle l_1 | \sqrt{\gamma^{\mathrm{D}}} \frac{-i}{\omega - \mathbf{H} + i\gamma/2} \sqrt{\gamma^{\mathrm{P}}} | l_2 \rangle. \quad (11)$$

Here ω is the frequency of the input light; $|l_1\rangle$ and $|l_2\rangle$ stand for the input light at sites l_1 and the output light at sites l_2. $\mathbf{H}$ is the coefficient matrix of the Hamiltonian H: $\langle l|\mathbf{H}|l'\rangle = H_{l,l'}$. $\gamma^{\mathrm{P/D/dis}} = \mathrm{diag}\{\gamma_{l_1}^{\mathrm{P/D/dis}}, \gamma_{l_2}^{\mathrm{P/D/dis}}, \ldots\}$ and $\gamma = \mathrm{diag}\{\gamma_{l_1}^{\mathrm{P}} + \gamma_{l_1}^{\mathrm{D}} + \gamma_{l_1}^{\mathrm{dis}}, \gamma_{l_2}^{\mathrm{P}} + \gamma_{l_2}^{\mathrm{D}} + \gamma_{l_2}^{\mathrm{dis}}, \ldots\}$ are the matrices of the pump/detection/dissipation and the total loss rates, respectively.

In our scheme, in principle, the input light can be injected into all sites due to such kind of 2D structure. It is worth stressing that, compared to the usual electrical detection in the solid system, this is the special advantage of simulating 3D material by using 2D structure and an extra synthetic dimension. It provides the possibility of mimicking a specific momentum by tuning the related phases of the input light at different sites. As we only care about the boundary states, it is sufficient to inject the light into the sites with $l_y = 1$ and l_x from 1 to N_x. Therefore, the input light takes the following form (at $l_y = 1$ only, unless otherwise specified):

$$\Psi_{\mathrm{in}}(l_y = 1) = \sum_{l_z,l_x} e^{ik_z l_z + ik_x l_x + ik_y l_y} |l_z, s\rangle, \quad (12)$$

with s denoting the "spin." Here we just simulate the momentum along the z and x directions, which are controlled by k_z and k_x, respectively, as shown in the formula. The construction of the input light is discussed in detail in Appendix B. Nevertheless, it should be noted that the momentum k_i $(i = x, y, z)$ defined here is essentially different from the momentum of light in free space. Here, the momentum refers to the momentum of the simulated particles, which can be tuned by controlling the relative phase between adjacent sites.

With this input light, the transmission coefficient becomes

$$t_{l,\Psi_{\mathrm{in}}}(\omega) = \langle l | \sqrt{\gamma^{\mathrm{D}}} \frac{-i}{\omega - \mathbf{H} + i\gamma/2} \sqrt{\gamma^{\mathrm{P}}} | \Psi_{\mathrm{in}} \rangle. \quad (13)$$

From this equation, one understands that $t_{l,\Psi_{\mathrm{in}}}(\omega)$ reaches its maximum value when ω is close to the eigenvalues of $\mathbf{H}$, and meanwhile $|\Psi_{\mathrm{in}}\rangle$ only couples to the corresponding eigenstates. This is just the resonance transmission, which means that the energy spectrum can be detected via $t_{l,\Psi_{\mathrm{in}}}(\omega)$. Nevertheless, the direct detection of $t_{l,\Psi_{\mathrm{in}}}(\omega)$ is possible but complex since the detection on a specific OAM l_z needs extra experimental methods [54]. Hence, in this work, we detect the total transmission of all the sites instead. It is obtained by the Landauer-Buiticker formula,

$$T = \mathrm{Tr}(t^\dagger t) = \sum_l |t_{l,\Psi_{\mathrm{in}}}|^2, \quad (14)$$

which is actually the intensity of the output light.

Considering the fact that a small system is much easier to realize in experiment, we investigate the transmission spectra in a small $N_x \times N_y$ cluster with a periodic boundary condition. The calculated transmission coefficient T as a function of k_z and energy ω at different k_x is presented in Figs. 3(a)–3(c), in which we see that the full band structure of the bulk can be clearly mapped out via the selection rules of energy and momenta. Here the input light is injected into the system at all sites with their phase irrelevant to l_y. Hence, the momentum along the y axis, i.e., k_y, is chosen to be zero. Moreover, it is necessary to emphasize that, in a small cluster, the value of k_x is restricted to several discrete values, i.e., $k_x = 2\pi n/N_x$, with $n = 0, 1, \ldots, N_x - 1$. However, since the value of k_z in the synthetic dimension can be very large, the band structure can still be clearly observed in experiment.

In addition, an extra benefit from such kind of synthetic photonic system is that one can easily detect the spin texture of the energy band. From the transmission coefficient, one can deduce that it will lead to a negligible response if the spin of the input light is orthogonal to that of the eigenstate of the system. Therefore, in Fig. 3, we not only scan the energy band by detecting the transmission rates but also investigate the spin texture. When $k_x = 0$, as shown in Fig. 3(a), we demonstrate two Weyl points at $k_z = \pm k_0$ along the z axis, as expected from Fig. 2(b). In this case, the spin directions in the band remain unchanged as k_z varies. On the other hand, for the cases of $k_x = 2\pi/3$ and $4\pi/3$ [see Figs. 3(b) and 3(c)], the spin directions of these states vary as k_z. To show the variation of the spin direction more clearly, we plot the results with only spin-up or only spin-down input light in the inset. It is noted that the obtained results for $k_x = 2\pi/3$ and $4\pi/3$ are the same; hence we only plot spin up in the inset in Fig. 3(b) and spin down in the inset in Fig. 3(c).

In such a synthetic system, the coefficients t_{xy}, t_y, t_z, and $t_{z'}$ are determined by the parameters of the main cavity and the BS (see Appendix A). Without loss of generality, they are set to be 1 in our calculation. Due to the topological stability, the variation of the parameters t_{xy}, t_y, t_z', and t_z have no essential effects on the Weyl points except changing their locations. This can be seen from Eq. (2), where the location of the Weyl points is only determined by t_z and t_z'. This means that our main results are robust against the variation of these parameters. To show this point more clearly, we plot the results under different t_{xy} (t_y and t_z with $k_0 = \pi/2$ are the same) and t_z' in Figs. 3(d)–3(f). We find that the variation of t_{xy} has little effect on the results while the variation of t_z' makes two Weyl points move closer to each other.

Under the open boundary condition, the edge modes will be detectable by measuring transmission spectra. In this system, since the chiralities of the Weyl points projected onto the x-z plane have the same sign, this ensures that they cannot be canceled by each other, giving rise to the twofold degenerate flat bands [see Fig. 2(b)]. The calculated transmission rate T obtained by scanning the momentum k_z and k_x under pumping eigen cavity-frequency (with zero shift) is presented in Fig. 3(g), in which the strong transmission indicates a resonance due to the presence of localized edge modes. Different from the result in the bulk [Fig. 3(a)], we find that the resonant transmission can always be found for all k_x at the same $k_z = \pm k_0$. The discrete value of k_x again is attributed to

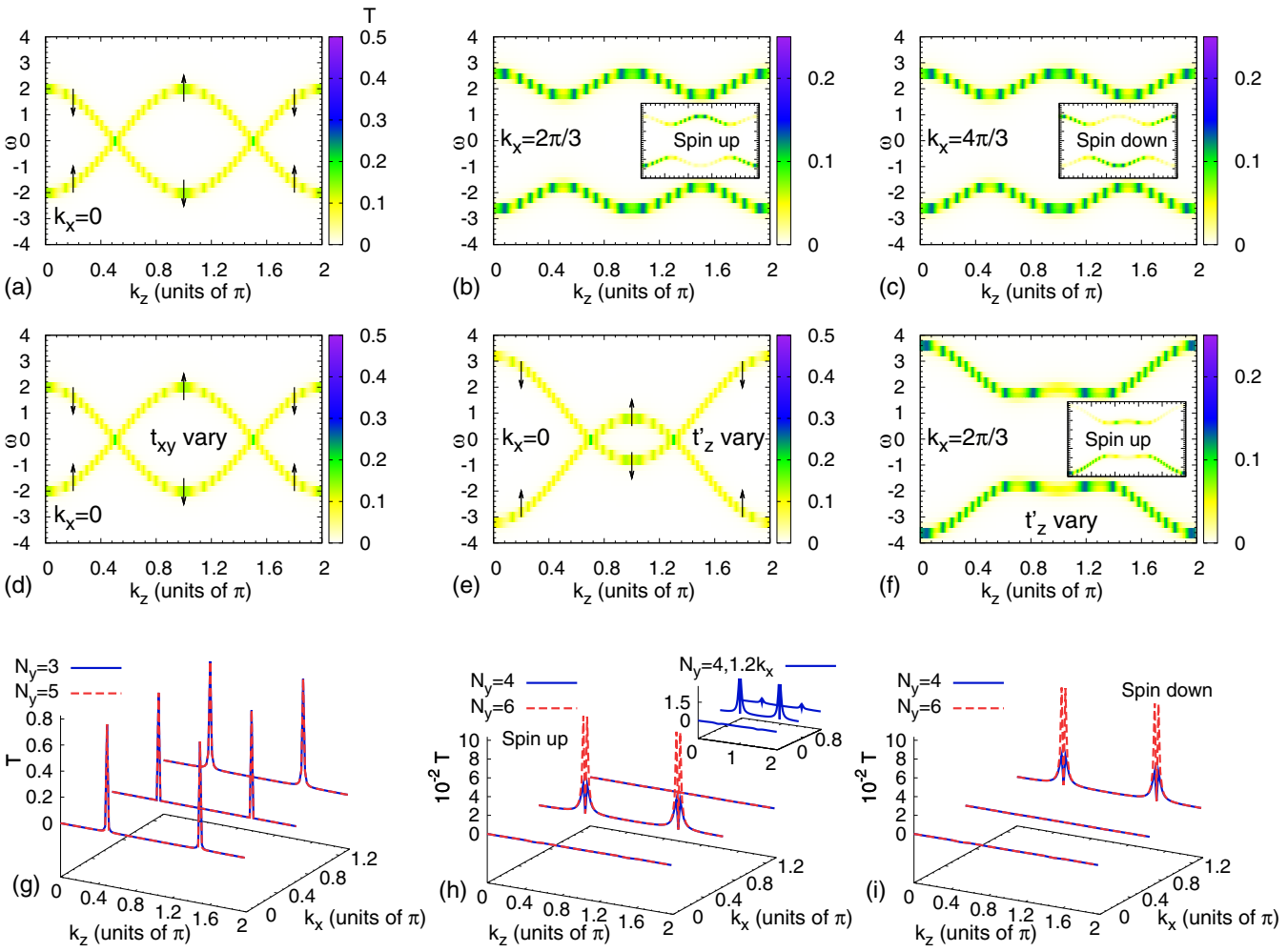

FIG. 3. Transmission rates along the z direction for the bulk system at (a) $k_x = 0$, (b) $k_x = 2\pi/3$, and (c) $k_x = 4\pi/3$. The results with only "spin-up" or "spin-down" input light are marked by the up and down arrows in panel (a) and shown in the insets in panels (b) and (c). (d) Transmission rates with $t_{xy} = 1.2$ with the other parameters being the same as those in panel (a). (e) and (f) $t'_z = -0.59$ with the other parameters being the same as those in panels (a) and (b), respectively. (g) Transmission rate in the momentum space with the y direction being the constrained direction. Here, $N_y = 3$ for blue curves and $N_y = 5$ for red curves. (h) Transmission rate with the spin of the input light being up. (i) Transmission rate with the 'spin of the input light being down. Here $N_y = 4$ or 6. The inset figure in panel (h) is the case with k_x being 1.2 times larger. In the calculation, $N_z = 100$, $N_x = 3$, $k_0 = \pi/2$, $\gamma_l^{\rm P} = \gamma_l^{\rm D} = 0.1 = 10\gamma_l^{\rm dis}$, and $t_{xy} = t_y = t_z = 1$.

the finite size of our system, and it will become a continuous Fermi arc when $N_x \to \infty$. This observation is independent of the spin of the input light.

The above observed phenomena depends strongly on the size of the system along the k_y direction, in which the edge states may be destroyed with a small energy splitting when N_y is even [see Figs. 3(h) and 3(i) where the strong resonant transmission is absent). This even-odd alternating behavior is a typical feature in finite-size systems [55]. In our model, the edge states have exactly zero energy when the size N_y is odd, and finite coupling between the edge states can be realized when N_y is even. Consider the following Hamiltonian at $k_z = k_0$:

$$H = \sum_{\mathbf{k}} \phi^\dagger_{k_x,l_y}(it_{xy}\sigma_x e^{ik_x} - it_y\sigma_y)\phi_{k_x,l_y+1} + \text{H.c.} \quad (15)$$

The band structures are determined by the following equations:

$$E\phi_{k_x,l_y} = (it_{xy}\sigma_x e^{ik_x} - it_y\sigma_y)\phi_{k_x,l_y+1} + (it_{xy}\sigma_x e^{ik_x} - it_y\sigma_y)^\dagger\phi_{k_x,l_y-1}, \quad l_y \neq 0, N_y, \quad (16)$$

$$E\phi_{k_x,1} = (it_{xy}\sigma_x e^{ik_x} - it_y\sigma_y)\phi_{k_x,2}, \quad (17)$$

$$E\phi_{k_x,N_y} = (it_{xy}\sigma_x e^{ik_x} - it_y\sigma_y)^\dagger\phi_{k_x,N_y-1}. \quad (18)$$

When N_y is odd, we find that eigenvalue with $E = 0$ is possible and the corresponding two degenerate wave functions are written as

$$\phi^\pm_{l_y} = \frac{1}{2}\begin{cases} \left(\frac{t_y^2 + t_{xy}^2 e^{-2ik_x}}{\xi_\pm}\right)^i \begin{pmatrix} 1 \pm 1 \\ 1 \mp 1 \end{pmatrix}, & l_y = 2i-1, \\ 0, & l_y = 2i, \end{cases} \quad (19)$$

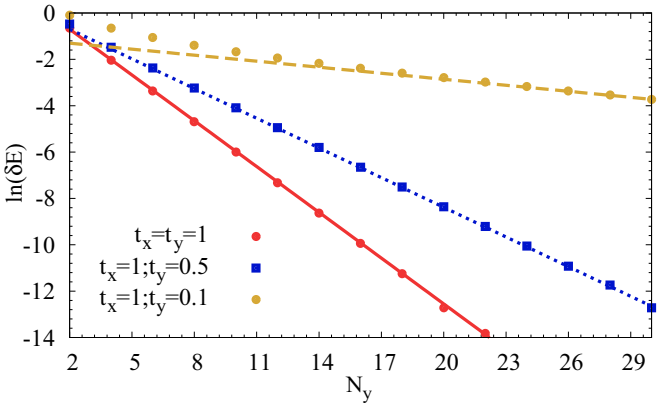

FIG. 4. Energy splitting induced by wave-function overlap between the two edge modes (see dots) in the case with even N_y. The lines represent the splitting determined by Eq. (20).

where $\xi_\pm = t_{xy}^2 + t_y^2 \mp 2t_x t_{xy} \sin k_x$. These two degenerate states possess different spin textures. However, through the resonance transmission, both of them lead to large transmission amplitude. On the other hand, when N_y is even, the zero energy localized states are coupled and their energy splitting is of the following form,

$$\delta E_{\text{edge}} \sim e^{-N_y \ln|\frac{\xi_+}{\xi_-}|/4}, \tag{20}$$

following the method in Ref. [56]. This accounts for the splitting of T observed in Figs. 3(h) and 3(i). The numerical verification of this result is presented in Fig. 4. The detailed numerical simulation also shows that the localized edge states depend strongly on the spin degrees of freedom and thus explains the strong spin-dependent effect in Figs. 3(h) and 3(i). We should also note here that the splitting obtained from our calculation in the case with $N_y = 4$ is $0.12t_{xy}$, with $t_{xy} = t_y = t_z$. This is larger than the dissipation $\gamma_l/2 = 0.105t_{xy}$. As a result, it leads to a much smaller transmission rate as shown in Figs. 3(h) and 3(i), which is experimentally resolvable.

Consider the imperfect momentum shift of the input light used in the experiment. If the deviation is small, the effect from the selected momentum will still be dominant. To show this point more clearly, we first calculate the case with k_x being 1.2 times larger than the ideal parameter. As shown in the inset of Fig. 3(h), besides the ideal resonance peak, an extra small peak appears at a different momentum value. On the other hand, if we change k_z from 0.5π to 0.38π, the corresponding transmission rate changes from 0.031 to 0.021. This is still much larger than the response away from the Weyl points, which means that it is still experimentally resolvable.

IV. SUMMARY

In summary, we have shown the potential value of taking advantage of the OAM property of the light to simulate the Weyl semimetal system. This approach is experimentally accessible since the required experimental techniques (i.e., reliable manipulation of the OAM states [47,54], design and operation of degenerate cavities [42–44], and locking of multiple optical cavities [57]) have been realized.

Furthermore, compared to the real solid material obtained recently, the platform based on photonic synthetic dimension provides a more flexible way of investigating the properties of the Weyl point. We show that, using the input-output relation, both the Dirac cone of the bulk system and the Fermi arcs on the surface can be easily detected. More interestingly, when the number of the sites in the constrained direction is odd, the boundary states in the two boundaries do not interact with each other. This means that to observe the Fermi arc, only a few sites is sufficient.

In addition, we also show the case with an even number of sites in the constrained direction. In this case, both the influence of the coupling between the boundary states and the strong k_x-dependent spin texture can be easily observed, which leads to a momentum-dependent transport property. These results further indicate that our system is a valuable system which is especially suitable for investigating the properties of the Weyl semimetals.

ACKNOWLEDGMENTS

This work was funded by the National Plan on Key Basic Research and Development (Grant No. 2016YFA0301700), the National Natural Science Foundation of China (Grant No. 11574294,61490711), and the Strategic Priority Research Program (B) of the Chinese Academy of Sciences (Grant No. XDB01030200). M.G. is supported by the National Youth Thousand Talents Program (Grant No. KJ2030000001), the USTC start-up funding (Grant No. KY2030000053), and the CUHK RGC (Grant No. 401113).

APPENDIX A: EXPRESSION OF THE HOPPING ENERGY

In this appendix, we show how to tune the value of t_y in Hamiltonian (1) in the main text. Since the other parameters (t_{xy} and t_z) can be obtained in the same way, for simplicity, we omit their derivation steps.

The hopping Hamiltonian along the y direction can be written as

$$H = it \sum_l e^{i2\pi\phi} \phi_l^\dagger \sigma^y \phi_{l+1} + \text{H.c.}, \tag{A1}$$

with σ^y being the Pauli matrix and t being the hopping energy.

To obtain the hopping energy, a basic idea is that we can take advantage of transfer matrix analysis [50] to derive the dispersion relation of the system. Then, we can get the hopping energy. The schematics of the hopping between sites l and $l+1$ is shown in Fig. 5, where we introduce the photon field amplitudes a_l, b_l, c_l, and d_l at site l. We further assume that the reflection and transmission coefficients of the BS is $r_e = i|r_e|$ and $t_r = |t_r|$, with $|r_e|^2 + |t_r|^2 = 1$. Then, the transfer matrix is written as

$$M_{\text{BS}} = \begin{pmatrix} \frac{1}{-i|r_e|} & \frac{t_r}{i|r_e|} \\ \frac{t_r}{-i|r_e|} & \frac{1}{i|r_e|} \end{pmatrix}. \tag{A2}$$

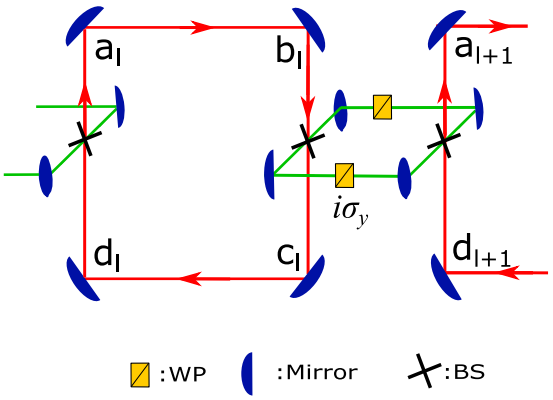

FIG. 5. Schematics on the model Hamiltonian, Eq. (A1). a_l, b_l, c_l, and d_l are the amplitudes of lights at the corresponding places shown in the figure at site l. The other elements are the same as those in Fig. 1.

Thus, the relation between the amplitudes in sites l and $l+1$ is obtained as

$$\begin{pmatrix} a_{l+1} \\ d_{l+1} \end{pmatrix} = \begin{pmatrix} e^{-iKS_c/8} & 0 \\ 0 & e^{iKS_c/8} \end{pmatrix} M_{\rm BS} \times \begin{pmatrix} e^{-iKS_a/2-2i\pi\phi} e^{i\alpha\cdot\sigma^y} & 0 \\ 0 & e^{iKS_a/2-2i\pi\phi} e^{i\alpha\cdot\sigma^y} \end{pmatrix} \times M_{\rm BS} \begin{pmatrix} e^{-iKS_c/8} & 0 \\ 0 & e^{iKS_c/8} \end{pmatrix} \begin{pmatrix} b_l \\ c_l \end{pmatrix} \tag{A3}$$

and

$$b_l = a_l e^{-iKS_c/4}, \quad d_l = c_l e^{-iKS_c/4}. \tag{A4}$$

Here $\alpha = (0,\pi/2,0)$, and S_c and S_a are the total optical path length of the main cavity and the coupling cavity. Moreover, K is the momentum of the light, which is different from the momentum k of the simulated particles in the system. This k appears in the Bloch theory which leads to the formula

$$\begin{pmatrix} a_{l+1} \\ b_{l+1} \\ c_{l+1} \\ d_{l+1} \end{pmatrix} = \begin{pmatrix} a_l \\ b_l \\ c_l \\ d_l \end{pmatrix} e^{-ik\Lambda}. \tag{A5}$$

Here, Λ is the unit spacing. With Eqs. (A3)–(A5), one obtains the relationship between k and K under the condition $t_r \sim 1$, i.e., $|r_e| \ll 1$, as [27]

$$|r_e|^2\sigma^y \sin(2\pi\phi - k\Lambda) \approx \cos[K(S_a - S_c)/2] - \cos[K(S_a + S_c)/2]. \tag{A6}$$

Since the length of the main cavity is constructive, and that of the auxiliary cavity is destructive, one understands that $KS_a = (2n+1)\pi + \Delta_K S_a$ and $KS_c = 2m\pi + \Delta_K S_c$, with n and m being integers. Here $\Delta_K = K - K_0$, with K_0 being the resonance momentum of the cavity and $\Delta_K S_a$ as well as $\Delta_K S_c$ being small. With this condition, one obtains

$$|r_e|^2\sigma^y \sin(2\pi\phi - k\Lambda) \approx (-1)^\nu \Delta_K S_c, \tag{A7}$$

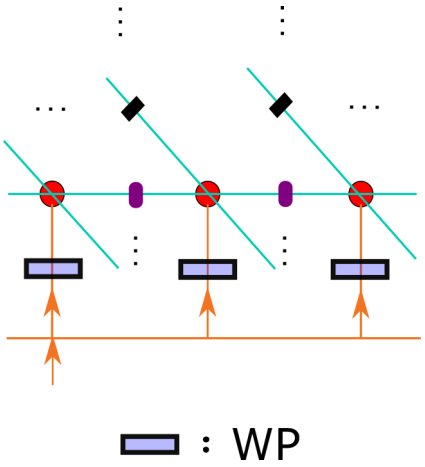

FIG. 6. Schematics on the input light (orange lines). The WPs are used to tune the relative phases of the cavities to simulate the particle momentum. The other elements are the same as those in Fig. 1.

with the integer ν depending on n and m. Here we take $\nu = 1$ and further use the relation $K = \omega/c$; then one obtains

$$|r_e|^2\sigma^y \sin(k\Lambda - 2\pi\phi) = (\omega - \omega_0)S_c/c. \tag{A8}$$

Here ω is the energy of the light and ω_0 is the resonance frequency of the cavity. Comparing this equation to the model Hamiltonian, one understands that the hopping energy

$$t = \frac{c|r_e|^2}{2S_c}. \tag{A9}$$

As for the parameter t_z', it is simulated by a WP, which tunes the resonance frequency of the main cavity, i.e.,

$$KS_c + \alpha_{t'}\sigma_z = 2\pi n, \tag{A10}$$

with n being an integer. Then, for the resonance frequency of spin up, it becomes

$$\omega_{0\uparrow} = \omega_0 - \alpha_{t'}c/S_c, \tag{A11}$$

with ω_0 being the resonance frequency without the WP. On the other hand, the resonance frequency of spin down is

$$\omega_{0\downarrow} = \omega_0 + \alpha_{t'}c/S_c. \tag{A12}$$

Hence,

$$t_z' = -\alpha_{t'}c/S_c. \tag{A13}$$

APPENDIX B: CONSTRUCTION OF k_z FOR THE INPUT LIGHT

In this appendix we discuss the construction of the input light. As shown in the main text, the input light needs to fulfill Eq. (12) to simulate the particle momentum. For the momentum in the x-y plane, this is easy to be realized by adding wave plates to tune the relative phases between cavities as shown in Fig. 6.

On the other hand, for the momentum in the z direction, this will be more difficult since the cavity is simulated by the OAM. It is well known that if the optical elements have

cylindrical symmetry, the solutions are the Laguerre-Gaussian (LG) modes $E_{p,l}(r,\phi)e^{-ikz}$ [58] with

$$E_{p,l}(r,\psi) = E_0 \frac{W_0}{W(z)} \left(\frac{r\sqrt{2}}{W(z)}\right)^{|l|} \mathcal{L}_p^{|l|}\left(\frac{2r^2}{W^2(z)}\right) e^{\frac{-r^2}{W^2(z)}} \times e^{\frac{-ikr^2}{2R(z)}} e^{i(2p+|l|+1)\zeta(z)} e^{il\psi}. \quad \text{(B1)}$$

Here $W(z) = W_0\sqrt{1+(z/z_0)^2}$, $R(z) = z[1+(z/z_0)^2]$, and $\zeta = \arctan(z/z_0)$, with $z_0 = \pi W_0^2/\lambda$, and $\mathcal{L}_p^{|l|}(x)$ is the generalized Laguerre polynomial. Thus, to simulate the momentum in the z direction, one only needs to generate the light with its transverse field being

$$E_t(k_z,r,\psi) = \sum_{l_z} e^{ik_z l_z} E_{0,l_z}(r,\psi). \quad \text{(B2)}$$

[1] X.-G. Wan, A. M. Turner, A. Vishwanath, and S. Y. Savrasov, Phys. Rev. B **83**, 205101 (2011).
[2] G. Xu, H. Weng, Z. Wang, X. Dai, and Z. Fang, Phys. Rev. Lett. **107**, 186806 (2011).
[3] A. A. Burkov and L. Balents, Phys. Rev. Lett. **107**, 127205 (2011).
[4] L. Lu, L. Fu, J. D. Joannopoulos, and M. Soljačić, Nat. Photon. **7**, 294 (2013).
[5] S.-M. Huang, S.-Y. Xu, I. Belopolski, C.-C. Lee, G. Chang, B. Wang, N. Alidoust, G. Bian, M. Neupane, C. Zhang, S. Jia, A. Bansil, H. Lin, and M. Z. Hasan, Nat. Commun. **6**, 7373 (2014).
[6] S.-Y. Xu, I. Belopolski, N. Alidoust, M. Neupane, G. Bian, C. Zhang, R. Sankar, G. Chang, Z. Yuan, C.-C. Lee, S.-M. Huang, H. Zheng, J. Ma, D. S. Sanchez, B. Wang, A. Bansil, F. Chou, P. P. Shibayev, H. Lin, S. Jia, and M. Z. Hasan, Science **349**, 613 (2015).
[7] B. Q. Lv, H. M. Weng, B. B. Fu, X. P. Wang, H. Miao, J. Ma, P. Richard, X. C. Huang, L. X. Zhao, G. F. Chen, Z. Fang, X. Dai, T. Qian, and H. Ding, Phys. Rev. X **5**, 031013 (2015).
[8] J. Ruan, S.-K. Jian, H. Yao, H. Zhang, S.-C. Zhang, and D. Xing, Nat. Commun. **7**, 11136 (2016).
[9] X. Huang, L. Zhao, Y. Long, P. Wang, D. Chen, Z. Yang, H. Liang, M. Xue, H. Weng, Z. Fang, X. Dai, and G. Chen, Phys. Rev. X **5**, 031023 (2015).
[10] C.-L. Zhang *et al.*, Nat. Commun. **7**, 10735 (2016).
[11] B. Sbierski, G. Pohl, E. J. Bergholtz, and P. W. Brouwer, Phys. Rev. Lett. **113**, 026602 (2014).
[12] P. Baireuther, J. M. Edge, I. C. Fulga, C. W. J. Beenakker, and J. Tworzydlo, Phys. Rev. B **89**, 035410 (2014).
[13] L. Wang, S.-K. Jian, and H. Yao, Phys. Rev. A **93**, 061801 (2016).
[14] J. Bravo-Abad, L. Lu, L. Fu *et al.*, 2D Mater. **2**, 034013 (2015).
[15] L. Lu *et al.*, Science **349**, 622 (2015).
[16] W.-J. Chen, M. Xiao, and C. T. Chan, Nat. Commun. **7**, 13038 (2015).
[17] H.-L. Wang, L. Zhou, and Y.-D. Chong, Phys. Rev. B **93**, 144114 (2016).
[18] W. Cao *et al.*, Nat. Commun. **7**, 12435 (2016).
[19] M. Xiao, Q. Lin, and S. Fan, Phys. Rev. Lett. **117**, 057401 (2016).
[20] M. Xiao, W.-J. Chen, W.-Y. He, and C. T. Chan, Nat. Phys. **11**, 920 (2015).
[21] Z. Yang and B. Zhang, Phys. Rev. Lett. **117**, 224301 (2016).
[22] F. Mei, Z.-Y. Xue, D.-W. Zhang, L. Tian, C. Lee, S.-L. Zhu, Quantum Sci. Technol. **1**, 015006 (2016).
[23] Q. Lin, M. Xiao, L. Yuan, and S. Fan, Nat. Commun. **7**, 13731 (2016).
[24] D. W. Zhang, Quantum Inf. Process. **15**, 4477 (2016).
[25] O. Boada, A. Celi, J. I. Latorre, and M. Lewenstein, Phys. Rev. Lett. **108**, 133001 (2012).
[26] A. Celi, P. Massignan, J. Ruseckas, N. Goldman, I. B. Spielman, G. Juzeliūnas, and M. Lewenstein, Phys. Rev. Lett. **112**, 043001 (2014).
[27] X.-W. Luo, X. Zhou, C.-F. Li, J.-S. Xu, G.-C. Guo, and Z.-W. Zhou, Nat. Commun. **6**, 7704 (2015).
[28] H. M. Price, T. Ozawa, and N. Goldman, Phys. Rev. A **95**, 023607 (2017).
[29] M. Mancini, G. Pagano, G. Cappellini, L. Livi, M. Rider, J. Catani, C. Sias, P. Zoller, M. Inguscio, M. Dalmonte, and L. Fallani, Science **349**, 1510 (2015).
[30] B. K. Stuhl, H. I. Lu, L. M. Aycock, D. Genkina, and I. B. Spielman, Science **349**, 1514 (2015).
[31] N. R. Cooper and A. M. Rey, Phys. Rev. A **92**, 021401(R) (2015).
[32] B. Gadway, Phys. Rev. A **92**, 043606 (2015).
[33] E. J. Meier, F. A. An, and B. Gadway, Phys. Rev. A **93**, 051602(R) (2016).
[34] L. F. Livi, G. Cappellini, M. Diem, L. Franchi, C. Clivati, M. Frittelli, F. Levi, D. Calonico, J. Catani, M. Inguscio, and L. Fallani, Phys. Rev. Lett. **117**, 220401 (2016).
[35] F. A. An, E. J. Meier, and B. Gadway, Sci. Adv. **3**, e1602685 (2017).
[36] M. Schmidt, S. Kessler, V. Peano, O. Painter, and F. Marquardt, Optica **2**, 635 (2015).
[37] T. Ozawa, H. M. Price, N. Goldman, O. Zilberberg, and I. Carusotto, Phys. Rev. A **93**, 043827 (2016).
[38] L. Yuan, Y. Shi, and S. Fan, Opt. Lett. **41**, 741 (2016).
[39] X.-W. Luo, X. Zhou, J.-S. Xu, C.-F. Li, G.-C. Guo, C. Zhang, and Z.-W. Zhou Nat. Commun. **8**, 16097 (2017).
[40] X. F. Zhou, X.-W. Luo, S. Wang, G.-C. Guo, X. Zhou, H. Pu, and Z.-W. Zhou, Phys. Rev. Lett. **118**, 083603 (2017).
[41] T. Ozawa and I. Carusotto, Phys. Rev. Lett. **118**, 013601 (2017).
[42] J. A. Arnaud, Appl. Opt. **8**, 189 (1969).
[43] B. Chalopin, A. Chiummo, C. Fabre, A. Matre, and N. Treps, Opt. Express **18**, 8033 (2010).
[44] Z.-D. Cheng *et al.*, Opt. Lett. **42**, 2042 (2017).
[45] A. Mair, A. Vaziri, G. Weihs, and A. Zeilinger, Nature (London) **412**, 313 (2001).
[46] W. M. Lee, X. C. Yuan, and W. C. Cheong, Opt. Lett. **29**, 1796 (2004).
[47] M. Malik, M. Mirhosseini, M. P. J. Lavery, J. Leach, M. J. Padgett, and R. W. Boyd, Nat. Commun. **5**, 3115 (2014).
[48] R. Fickler, R. Lapkiewicz, W. N. Plick, M. Krenn, C. Schaeff, S. Ramelow, and A. Zeilinger, Science **338**, 640 (2012).

[49] M. Krenna, M. Huberc, R. Fickler, R. Lapkiewicza, S. Ramelowa, and A. Zeilinger, Proc. Natl. Acad. Sci. USA **111**, 6243 (2014).
[50] A. Yariv and P. Yeh, *Photonics: Optical Electronics in Modern Communications* (Oxford University Press, London, 2007).
[51] S. S. R. Oemrawsingh, J. A. W. van Houwelingen, E. R. Eliel, J. P. Woerdman, E. J. K. Verstegen, J. G. Kloosterboer, and G. W. 't Hooft, Appl. Opt. **43**, 688 (2004).
[52] S. S. R. Oemrawsingh, X. Ma, D. Voigt, A. Aiello, E. R. Eliel, G. W. 't Hooft, and J. P. Woerdman, Phys. Rev. Lett. **95**, 240501 (2005).
[53] D. F. Walls and G. J. Milburn, *Quantum Optics* (Springer-Verlag, Berlin, 2008).
[54] A. M. Yao and M. J. Padgett, Adv. Opt. Photon. **3**, 161 (2011).
[55] Y. Zhou and M. W. Wu, J. Phys.: Condens. Matter **26**, 065801 (2014).
[56] A. Y. Kitaev, Phys.-Usp. **44**, 131 (2001).
[57] X. Su, Y. Zhao, S. Hao, X. Jia, C. Xie, and K. Peng, Opt. Lett. **37**, 5178 (2012).
[58] N. Hodgson and H. Weber, *Laser Resonators and Beam Propagation* (Springer, New York, 2005).